



# Measurement of the CKM angle $\gamma$ using $B_s^0 \rightarrow D_s^+ K \pi \pi$ decays

LHCb collaboration<sup>†</sup>

## Abstract

Guidelines for the preparation of LHCb documents are given. This is a “living” document that should reflect our current practice. It is expected that these guidelines are implemented for papers before they go into the first collaboration wide review. Please contact the Editorial Board chair if you have suggestions for modifications. This is the title page for journal publications (PAPER). For a CONF note or ANA note, switch to the appropriate template by uncommenting the corresponding line in the file `main.tex`.

Submitted to JHEP / Phys. Rev. D / Phys. Rev. Lett. / Phys. Lett. B / Eur. Phys. J. C  
/ Nucl. Phys. B

© 2018 CERN for the benefit of the LHCb collaboration. CC-BY-4.0 licence.

---

<sup>†</sup>Authors are listed at the end of this paper.



# 1 Detector and simulation

The LHCb detector [1,2] is a single-arm forward spectrometer covering the pseudorapidity range  $2 < \eta < 5$ , designed for the study of particles containing  $b$  or  $c$  quarks. The detector includes a high-precision tracking system consisting of a silicon-strip vertex detector surrounding the  $pp$  interaction region [3], a large-area silicon-strip detector located upstream of a dipole magnet with a bending power of about 4 Tm, and three stations of silicon-strip detectors and straw drift tubes [4,5] placed downstream of the magnet. The polarity of the dipole magnet can be reversed, which is done periodically throughout the data-taking process to control systematic asymmetries. The tracking system provides a measurement of the momentum,  $p$ , of charged particles with a relative uncertainty that varies from 0.5% at low momentum to 1.0% at 200 GeV/ $c$ . The minimum distance of a track to a primary vertex (PV), the impact parameter (IP), is measured with a resolution of  $(15 + 29/p_T) \mu\text{m}$ , where  $p_T$  is the component of the momentum transverse to the beam, in GeV/ $c$ . Different types of charged hadrons are distinguished using information from two ring-imaging Cherenkov detectors [6]. The online event selection is performed by a trigger [7], which consists of a hardware stage, based on information from the calorimeter and muon systems, followed by a software stage, which applies a full event reconstruction.

At the hardware trigger stage, events are required to have a muon with high  $p_T$  or a hadron, photon or electron with high transverse energy in the calorimeters. For hadrons, the transverse energy threshold is 3.5 GeV. The software trigger requires a two-, three- or four-track secondary vertex with a significant displacement from any primary  $pp$  interaction vertex. At least one charged particle must have a transverse momentum  $p_T > 1.6 \text{ GeV}/c$  and be inconsistent with originating from a PV. A multivariate algorithm [8] is used for the identification of secondary vertices consistent with the decay of a  $b$  hadron.

Simulation is necessary to model the effects of the detector acceptance and to optimize the selection requirements. In the simulation,  $pp$  collisions are generated using PYTHIA [9] with a specific LHCb configuration [10]. Decays of hadrons are described by EVTGEN [11], in which final-state radiation is generated using PHOTOS [12]. The interaction of the generated particles with the detector, and its response, are implemented using the GEANT4 toolkit [13] as described in Ref. [14].

## 2 Fit to invariant mass distribution of the $B_s^0 \rightarrow D_s^+ h \pi \pi$ candidates

Probability density functions (PDFs) are used to describe the signal and background components of the invariant mass distributions of  $B_s^0 D_s^+ \pi \pi \pi$  and  $B_s^0 \rightarrow D_s^+ K \pi \pi$  candidates. They are obtained from a mixture of data-driven approaches and simulation, where the simulated distributions are corrected for kinematic differences between the simulation and data.

The shape of the signal candidates in the  $B_s^0 \rightarrow D_s^+ K \pi \pi$  and  $B_s^0 \rightarrow D_s^+ \pi \pi \pi$  distributions are modelled using a Johnson's SU function [15], which results from a variable transformation of a normal distribution to allow for asymmetric tails. It provides a good description of the Gaussian signal peak, as well as reconstruction effects and radiative tails of the distribution. The shape of the Johnson's SU function is determined using simulation for both modes and subsequently fixed in the fit to data. To compensate small differences

between the simulation and data, scale factors for the mean and width of the PDFs are introduced and floated during the fit. For the functional form of the combinatorial background, second order polynomials are used whose parameters are determined, for each  $D_s^+$  mode separately, in the fit to data. The partially reconstructed background component is described using an empirical description that is derived from simulation. In the fit to  $B_s^0 D_s^+ \pi \pi \pi$  data, all parameters are fixed to the ones obtained from simulation, except for a width parameter to account for small discrepancies between data and simulated samples. For the fit to  $B_s^0 D_s^+ K \pi \pi$  data, the shape is fixed to the one obtained from the control mode. A small fraction of  $B_s^0 D_s^+ \pi \pi \pi$  and  $B_s^0 D_s^{+*} \pi \pi \pi$  decays, where one of the pions is misidentified as a kaon, contaminate the  $B_s^0 \rightarrow D_s^+ K \pi \pi$  data sample. Simulated samples of the control mode is used to determine the shape of this background, where the mass hypothesis of one pion is changed to a kaon during the reconstruction process. The yield of this component is estimated from simulation and fixed in the fit to  $B_s^0 \rightarrow D_s^+ K \pi \pi$  data, taking into account the misidentification probability given the particle identification requirements imposed during the selection process.

Figure 1 shows the result of the fit to the invariant mass distributions of  $B_s^0 \rightarrow D_s^+ \pi \pi \pi$  and  $B_s^0 \rightarrow D_s^+ K \pi \pi$  candidates, where the data from Run I and II, as well as all  $D_s^+$  decay modes, are overlaid.

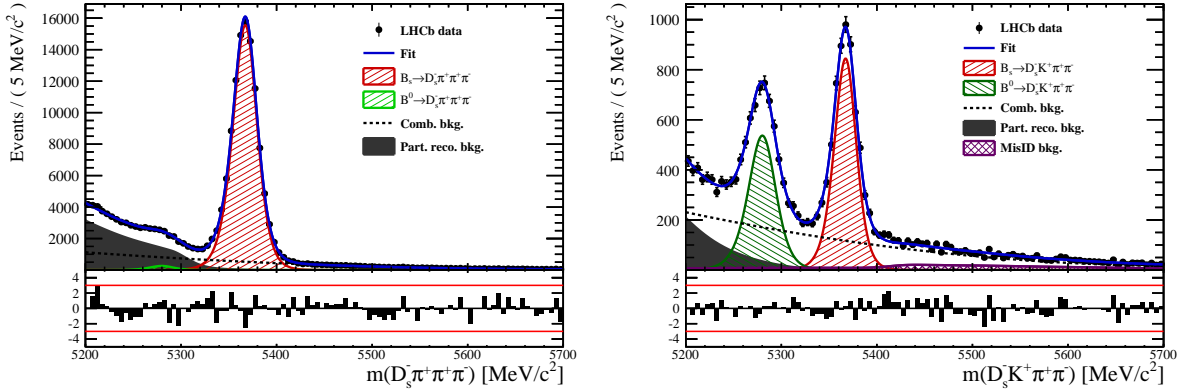


Figure 1: Invariant mass distribution of  $B_s^0 \rightarrow D_s^+ \pi \pi \pi$  (left) and  $B_s^0 \rightarrow D_s^+ K \pi \pi$  (right) candidates. The fit described in the text is overlaid.

### 3 Selection of signal candidates

### 4 Flavour tagging

To identify the initial flavour state of the  $B_s^0$  meson, a number of flavour tagging algorithms are used that either exploit the pair-wise production of  $b$  quarks and determine the flavour of the non-signal  $b$ -hadron produced in the event (opposite site, OS) or use particles produced in the fragmentation of the signal candidate  $B_s^0/\bar{B}_s^0$  (same side, SS). The same side kaon tagger searches for the charge of an additional kaon that accompanies the fragmentation of the signal  $B_s^0$  or  $\bar{B}_s^0$  candidate [16]. For the opposite site tagger [17], five different tagging algorithms are chosen: the algorithms that use the charge of an electron or a muon from semi-leptonic B decays, the tagger that uses the charge of a kaon from a  $b$

→ c → s decay chain, the algorithm which reconstructs opposite-side charm hadrons from a number of c-decays and the algorithm that determines the  $B_s^0/\bar{B}_s^0$  candidate flavour from the charge of a secondary vertex, reconstructed from the OS b-decay product. All five taggers are then combined into a single OS tagger.

Every tagging algorithm is prone to misidentify the signal candidate at a certain mistag rate  $\omega = (\text{wrong tags})/(\text{all tags})$ . This might be caused by particle misidentification, flavour oscillation of the neutral opposite site B-meson or by the selection of tracks from the underlying event. An imperfect determination of the  $B_s^0$  production flavour dilutes the observed  $CP$  asymmetry by  $D_{tag} = 1 - 2\omega$ . Therefore, the statistical precision with which the  $CP$  asymmetry can be measured scales as the inverse square root of the effective tagging efficiency:

$$\epsilon_{eff} = \epsilon_{tag}(1 - 2\omega)^2, \quad (1)$$

where  $\epsilon_{tag}$  is the fraction of tagged signal candidates.

For each  $B_s^0/\bar{B}_s^0$  candidate, the tagging algorithms provide a prediction for the mistag probability  $\eta$  based on the output of neural networks that take various variables, such as the kinematics of the tagging particles, as input. These are trained on either simulated or **sWeighted** samples of flavour specific control channels ( $B_s^0 \rightarrow D_s^- \pi^+$  (SS algorithm) and  $B^+ \rightarrow J/\psi K^+$  (OS algorithms)) and are optimized for highest  $\epsilon_{eff}$  on data. Utilizing flavour-specific final states, the estimated mistag  $\eta$  of each tagger has to be calibrated to match the actual mistag probability  $\omega$ . For the calibration, a linear model

$$\omega(\eta) = p_0 + p_1 \cdot (\eta - \langle \eta \rangle), \quad (2)$$

is used where  $\langle \eta \rangle$  is the average estimated mistag probability. A perfectly calibrated tagger would lead to  $\omega(\eta) = \eta$  and one would expect  $p_1 = 1$  and  $p_0 = \langle \eta \rangle$ . Due to the different interaction cross-sections of oppositely charged kaons, the tagging calibration parameters depend on the initial state flavour of the  $B_s^0$ . Therefore, the flavour asymmetry parameters  $\Delta p_0$ ,  $\Delta p_1$  and  $\Delta \epsilon_{tag}$  are introduced and defined as the difference of the corresponding values for  $B_s^0$  and  $\bar{B}_s^0$  mesons.

Table 1: The flavour tagging performances for the used OS taggers for Run-I data.

Tagger	$\epsilon$	$\omega$	$\epsilon\langle D^2 \rangle = \epsilon(1 - 2\omega)^2$
OS $\mu$	$(8.713 \pm 0.206)\%$	$(28.893 \pm 0.180(\text{stat}) \pm 2.291(\text{cal}))\%$	$(1.553 \pm 0.045(\text{stat}) \pm 0.337(\text{cal}))\%$
OS $e$	$(3.201 \pm 0.129)\%$	$(28.792 \pm 0.363(\text{stat}) \pm 3.611(\text{cal}))\%$	$(0.576 \pm 0.030(\text{stat}) \pm 0.196(\text{cal}))\%$
OS $K$	$(32.230 \pm 0.342)\%$	$(38.451 \pm 0.093(\text{stat}) \pm 1.145(\text{cal}))\%$	$(1.719 \pm 0.033(\text{stat}) \pm 0.341(\text{cal}))\%$
Vertex Charge	$(21.855 \pm 0.302)\%$	$(35.712 \pm 0.091(\text{stat}) \pm 1.474(\text{cal}))\%$	$(1.785 \pm 0.033(\text{stat}) \pm 0.368(\text{cal}))\%$

Table 2: The flavour tagging performances for the used OS taggers for Run-II data.

Tagger	$\epsilon$	$\omega$	$\epsilon\langle D^2 \rangle = \epsilon(1 - 2\omega)^2$
OS $\mu$	$(9.664 \pm 0.151)\%$	$(30.911 \pm 0.115(\text{stat}) \pm 1.369(\text{cal}))\%$	$(1.409 \pm 0.028(\text{stat}) \pm 0.202(\text{cal}))\%$
OS $e$	$(4.590 \pm 0.107)\%$	$(33.577 \pm 0.140(\text{stat}) \pm 2.007(\text{cal}))\%$	$(0.495 \pm 0.014(\text{stat}) \pm 0.121(\text{cal}))\%$
OS $K$	$(20.185 \pm 0.205)\%$	$(36.918 \pm 0.071(\text{stat}) \pm 0.969(\text{cal}))\%$	$(1.382 \pm 0.021(\text{stat}) \pm 0.205(\text{cal}))\%$
Vertex Charge	$(20.597 \pm 0.207)\%$	$(34.751 \pm 0.075(\text{stat}) \pm 0.961(\text{cal}))\%$	$(1.916 \pm 0.027(\text{stat}) \pm 0.242(\text{cal}))\%$
OS $c$	$(5.500 \pm 0.116)\%$	$(32.581 \pm 0.092(\text{stat}) \pm 1.848(\text{cal}))\%$	$(0.668 \pm 0.016(\text{stat}) \pm 0.142(\text{cal}))\%$

The OS electron, muon, kaon, charm and the secondary vertex charge tagging algorithms are individually calibrated and then combined into a single OS tagger. We choose

the flavour specific decay  $B_s \rightarrow D_s \pi \pi \pi$  as calibration mode due to the portability to the signal mode since its similarity with the  $B_s \rightarrow D_s K \pi \pi$  decay. The calibration is performed separately for Run-I and Run-II data, while the OS-c tagger is not included for Run-I data since the statistics is too low. Tables 1 and 2 list the measured tagging performances. The combined OS and SS-Kaon taggers are calibrated simultaneously by means of a fit to the decay-time distribution of background-subtracted  $B_s \rightarrow D_s \pi \pi \pi$  candidates, as discussed in Sec. 7. In this fit, the predicted mistag probabilities  $\eta_{OS}$  and  $\eta_{SS}$  are included as per-event observables, effectively giving a larger weight to the events that have a lower mistag probability. The tagger responses are combined into a single response on an event-by-event basis during the fit. Tables 3 and 4 report the tagging performances for the OS and SS combination considering three mutually exclusive categories of tagged events: OS only, SS only and both OS and SS. The tagging calibration parameters are listed in Table 5.

Table 3: The flavour tagging performances for only OS tagged, only SS tagged and both OS and SS tagged events for Run-I data.

$B_s \rightarrow D_s \pi \pi \pi$	$\epsilon_{tag}[\%]$	$\langle \omega \rangle [\%]$	$\epsilon_{eff}[\%]$
Only OS	$14.74 \pm 0.11$	$39.09 \pm 0.80$	$1.25 \pm 0.16$
Only SS	$35.38 \pm 0.18$	$44.26 \pm 0.62$	$1.05 \pm 0.18$
Both OS-SS	$33.04 \pm 0.30$	$37.33 \pm 0.73$	$3.41 \pm 0.33$
Combined	$83.16 \pm 0.37$	$40.59 \pm 0.70$	$5.71 \pm 0.40$

Table 4: The flavour tagging performances for only OS tagged, only SS tagged and both OS and SS tagged events for Run-II data.

$B_s \rightarrow D_s \pi \pi \pi$	$\epsilon_{tag}[\%]$	$\langle \omega \rangle [\%]$	$\epsilon_{eff}[\%]$
Only OS	$11.78 \pm 0.05$	$37.01 \pm 0.51$	$1.15 \pm 0.07$
Only SS	$41.28 \pm 0.10$	$42.65 \pm 0.35$	$1.79 \pm 0.12$
Both OS-SS	$28.62 \pm 0.15$	$35.35 \pm 0.40$	$3.63 \pm 0.16$
Combined	$81.68 \pm 0.19$	$39.28 \pm 0.40$	$6.57 \pm 0.21$

## 5 Decay-time resolution

The CP-violating parameters measured in the time-dependent fit are prone to dilution due to the fast  $B_s^0$ - $\bar{B}_s^0$  oscillation frequency, which is of the same order as the average decay-time resolution of the LHCb detector of  $\mathcal{O}(50 \text{ fs}^{-1})$  [2]. Therefore, it is crucial to correctly describe the decay-time resolution in order to accurately measure time-dependent CP violation. In particular, the parameters related to the amplitudes of the sine and cosine terms in Equation xXx are highly correlated to the chosen resolution model. Since the time resolution depends on the particular event, especially the decay time itself, the sensitivity on the CP parameters can be significantly improved by using an event-dependent model rather than an average resolution. For this purpose, the signal PDF is convolved with a Gaussian resolution function that has a different width for each candidate, obtained from the global kinematic fit to the  $B_s^0$  vertex and the  $D_s^+$  mass. To ensure the correct application, the per-candidate decay-time uncertainty  $\sigma_t$  has to be calibrated to match

the effective decay-time resolution observed in data,  $\sigma(\sigma_t)$ .

For data taken during Run I, a study of simulated  $B_s^0 \rightarrow D_s^+ K \pi \pi$  events is used to confirm the portability of the calibration relation determined in the closely related analysis of  $B_s^0 \rightarrow D_s^+ K$  decays [18]. The spread of the difference between the reconstructed and true decay time,  $\Delta t = t - t_{\text{true}}$ , follows the shape of a double Gaussian distribution and is a direct measure of the effective decay-time resolution for simulated events. The resulting two Gaussian widths are combined to calculate the dilution  $\mathcal{D}$ , which describes the effective damping of the CP amplitudes due to the finite time resolution:

$$\mathcal{D} = f_1 e^{-\sigma_1^2 \Delta m_s^2 / 2} + (1 - f_1) e^{-\sigma_2^2 \Delta m_s^2 / 2}, \quad (3)$$

where  $\sigma_1$  and  $\sigma_2$  are the widths of the Gaussians,  $f_1$  is the relative fraction of events described by the first Gaussian relative to the second and  $\Delta m_s$  is the oscillation frequency of  $B_s^0$  mesons. An effective single Gaussian width is calculated from the dilution as,

$$\sigma_{eff} = \sqrt{(-2/\Delta m_s^2) \ln \mathcal{D}}, \quad (4)$$

which converts the resolution into a single-Gaussian function with an effective resolution that causes the same damping effect on the magnitude of the  $B_s$  oscillation. The calibration relation is found to be portable between the  $B_s^0 \rightarrow D_s^+ K$  and  $B_s^0 \rightarrow D_s^+ K \pi \pi$  decay channels and thus it is used for data taken in Run I.

For data taken during Run II, the calibration is performed using a sample of prompt  $D_s^+$  mesons, combined with a kaon and two pions originating from the primary vertex to form 'fake'  $B_s^0$  candidates with a lifetime of  $t = 0$  by construction. The spread of observed decay times of the 'fake' candidates is described by a double Gaussian function, where only negative decay times are used to determine the effective resolution to avoid uncertainties introduced by physical backgrounds. Following the same approach used for data taken during Run I, the effective resolution is calculated from the dilution  $\mathcal{D}$ .

## 6 Decay-time acceptance

The decay-time distribution of the  $B_s^0$  mesons is distorted due to the geometry of the LHCb detector and the applied selections, described in Section 3. In particular, any requirement on the flight distance, the impact parameter or the direction angle (DIRA) of the  $B_s^0$  mesons leads to a decay-time dependent efficiency  $\epsilon(t)$ . This acceptance effect in the  $B_s^0 \rightarrow D_s^+ K \pi \pi$  decay-time distribution is strongly correlated with the CP parameters. However, for the flavour-specific control channel  $B_s^0 \rightarrow D_s^+ \pi \pi \pi$ , the acceptance can be measured since all CP-violating parameters are fixed to zero or unity. Using  $\Gamma_s$  as input, the parameters of the acceptance shape, as well as  $\Delta m_s$ , is measured using a time-dependent fit to the background-subtracted decay-time distribution of  $B_s^0 \rightarrow D_s^+ \pi \pi \pi$  candidates. To correct small differences between the signal and the control sample, the fit is performed simultaneously to the decay-time distributions of simulated  $B_s^0 \rightarrow D_s^+ \pi \pi \pi$ ,  $B_s^0 \rightarrow D_s^+ K \pi \pi$ , as well as to  $B^0 \rightarrow D_s^+ K \pi \pi$  data candidates. For all samples, the acceptance is parametrized using segments of cubic b-splines, which are implemented into the decay-time PDF in an analytic way [19]. The decay-time distribution of background-subtracted  $B_s^0 \rightarrow D_s^+ \pi \pi \pi$  data candidates, as well as the time-dependent fit to determine the acceptance shape, is shown in Figure 2.

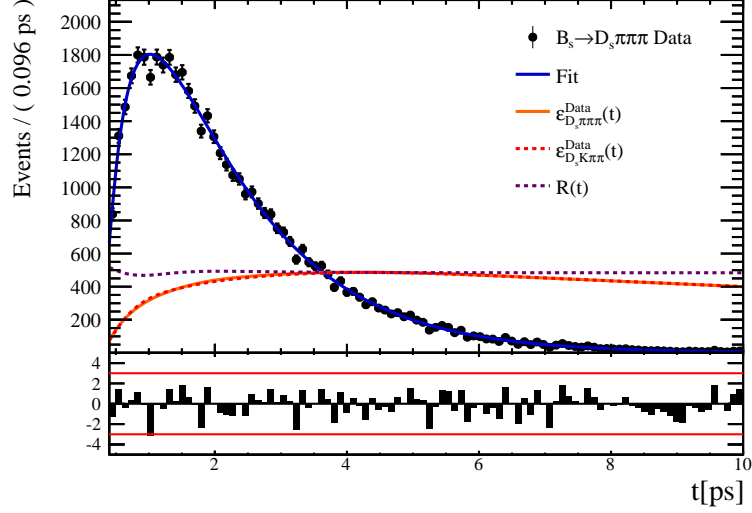


Figure 2: Decay-time distribution of background-subtracted  $B_s^0 \rightarrow D_s^+ \pi \pi \pi$  data. The fit to determine the shape of the time-dependent efficiency is overlaid, where the acceptance function is shown in an arbitrary scale.

## 7 Decay-time fit to $B_s^0 \rightarrow D_s^+ \pi \pi \pi$ and $B_s^0 \rightarrow D_s^+ K \pi \pi$ candidates

Table 5: Parameters determined from a fit to the  $B_s \rightarrow D_s \pi \pi \pi$  decay-time distribution. The uncertainties are statistical and systematic, respectively.

Fit Parameter	Run-I	Run-II
$p_0^{OS}$	$0.398 \pm 0.010 \pm 0.010$	$0.372 \pm 0.005 \pm 0.005$
$p_1^{OS}$	$0.895 \pm 0.085 \pm 0.090$	$0.788 \pm 0.043 \pm 0.030$
$\Delta p_0^{OS}$	$0.030 \pm 0.011 \pm 0.002$	$0.008 \pm 0.006 \pm 0.001$
$\Delta p_1^{OS}$	$0.011 \pm 0.095 \pm 0.017$	$0.067 \pm 0.052 \pm 0.002$
$\epsilon_{\text{tag}}^{OS} [\%]$	$47.775 \pm 0.365 \pm 0.067$	$40.399 \pm 0.182 \pm 0.029$
$\Delta \epsilon_{\text{tag}}^{OS} [\%]$	$0.016 \pm 1.353 \pm 0.097$	$0.316 \pm 0.618 \pm 0.046$
$p_0^{SS}$	$0.444 \pm 0.008 \pm 0.005$	$0.428 \pm 0.004 \pm 0.002$
$p_1^{SS}$	$0.949 \pm 0.111 \pm 0.067$	$0.787 \pm 0.039 \pm 0.025$
$\Delta p_0^{SS}$	$-0.019 \pm 0.009 \pm 0.001$	$-0.017 \pm 0.004 \pm 0.000$
$\Delta p_1^{SS}$	$0.064 \pm 0.124 \pm 0.017$	$0.028 \pm 0.048 \pm 0.006$
$\epsilon_{\text{tag}}^{SS} [\%]$	$68.426 \pm 0.340 \pm 0.013$	$69.903 \pm 0.170 \pm 0.007$
$\Delta \epsilon_{\text{tag}}^{SS} [\%]$	$-0.046 \pm 1.242 \pm 0.082$	$-0.319 \pm 0.575 \pm 0.062$
$A_P [\%]$	-0.045 (fixed)	$-0.183 \pm 0.642 \pm 0.048$
$\Delta m_s [\text{ps}^{-1}]$	$\text{xx.xx} \pm 0.0084 \pm 0.0058$	



Table 6:  $CP$  coefficients determined from a fit to the  $B_s \rightarrow D_s K \pi \pi$  decay-time distribution. The uncertainties are statistical and systematic, respectively.

Fit Parameter	Value
$C$	$x.xx \pm 0.12 \pm 0.02$
$D$	$x.xx \pm 0.32 \pm 0.08$
$\bar{D}$	$x.xx \pm 0.30 \pm 0.08$
$S$	$x.xx \pm 0.17 \pm 0.04$
$\bar{S}$	$x.xx \pm 0.17 \pm 0.04$

## References

- [1] LHCb collaboration, A. A. Alves Jr. *et al.*, *The LHCb detector at the LHC*, JINST **3** (2008) S08005.
- [2] LHCb collaboration, R. Aaij *et al.*, *LHCb detector performance*, Int. J. Mod. Phys. **A30** (2015) 1530022, [arXiv:1412.6352](#).
- [3] R. Aaij *et al.*, *Performance of the LHCb Vertex Locator*, JINST **9** (2014) P09007, [arXiv:1405.7808](#).
- [4] R. Arink *et al.*, *Performance of the LHCb Outer Tracker*, JINST **9** (2014) P01002, [arXiv:1311.3893](#).
- [5] P. d'Argent *et al.*, *Improved performance of the LHCb Outer Tracker in LHC Run 2*, JINST **9** (2017) P11016, [arXiv:1708.00819](#).
- [6] M. Adinolfi *et al.*, *Performance of the LHCb RICH detector at the LHC*, Eur. Phys. J. **C73** (2013) 2431, [arXiv:1211.6759](#).
- [7] R. Aaij *et al.*, *The LHCb trigger and its performance in 2011*, JINST **8** (2013) P04022, [arXiv:1211.3055](#).
- [8] V. V. Gligorov and M. Williams, *Efficient, reliable and fast high-level triggering using a bonsai boosted decision tree*, JINST **8** (2013) P02013, [arXiv:1210.6861](#).
- [9] T. Sjöstrand, S. Mrenna, and P. Skands, *PYTHIA 6.4 physics and manual*, JHEP **05** (2006) 026, [arXiv:hep-ph/0603175](#); T. Sjöstrand, S. Mrenna, and P. Skands, *A brief introduction to PYTHIA 8.1*, Comput. Phys. Commun. **178** (2008) 852, [arXiv:0710.3820](#).
- [10] I. Belyaev *et al.*, *Handling of the generation of primary events in GAUSS, the LHCb simulation framework*, Nuclear Science Symposium Conference Record (NSS/MIC) **IEEE** (2010) 1155.
- [11] D. J. Lange, *The EvtGen particle decay simulation package*, Nucl. Instrum. Meth. **A462** (2001) 152.
- [12] P. Golonka and Z. Was, *PHOTOS Monte Carlo: A precision tool for QED corrections in Z and W decays*, Eur. Phys. J. **C45** (2006) 97, [arXiv:hep-ph/0506026](#).
- [13] Geant4 collaboration, J. Allison *et al.*, *Geant4 developments and applications*, IEEE Trans. Nucl. Sci. **53** (2006) 270; Geant4 collaboration, S. Agostinelli *et al.*, *Geant4: A simulation toolkit*, Nucl. Instrum. Meth. **A506** (2003) 250.
- [14] M. Clemencic *et al.*, *The LHCb simulation application, Gauss: Design, evolution and experience*, J. Phys. Conf. Ser. **331** (2011) 032023.
- [15] N. L. Johnson, *Systems of frequency curves generated by methods of translation*, Biometrika **36** (1949) 149.

- 201 [16] LHCb, R. Aaij *et al.*, *A new algorithm for identifying the flavour of  $B_s^0$  mesons at*  
202 *LHCb*, JINST **11** (2016) P05010, [arXiv:1602.07252](#).
- 203 [17] LHCb collaboration, R. Aaij *et al.*, *Opposite-side flavour tagging of  $B$  mesons at the*  
204 *LHCb experiment*, Eur. Phys. J. **C72** (2012) 2022, [arXiv:1202.4979](#).
- 205 [18] LHCb, R. Aaij *et al.*, *Measurement of  $CP$  asymmetry in  $B_s^0 \rightarrow D_s^\mp K^\pm$  decays*, JHEP  
206 **03** (2018) 059, [arXiv:1712.07428](#).
- 207 [19] T. M. Karbach, G. Raven, and M. Schiller, *Decay time integrals in neutral meson*  
208 *mixing and their efficient evaluation*, [arXiv:1407.0748](#).